CHEMISTRY OF MATERIALS

Article

pubs.acs.org/cm

Ion-Exchange and Cation Solvation Reactions in Ti_3C_2 MXene

Michael Ghidiu,[†] Joseph Halim,[†,§] Sankalp Kota,[†] David Bish,[‡] Yury Gogotsi,[†,∥] and Michel W. Barsoum*[,†]

[†]Department of Materials Science and Engineering, Drexel University, Philadelphia, Pennsylvania 19104, United States

[‡]Department of Geological Sciences, Indiana University, Bloomington, Indiana 47405, United States

[§]Thin Film Physics Division, Department of Physics, Chemistry and Biology (IFM), Linköping University, SE-58183 Linköping, Sweden

[∥]A. J. Drexel Nanomaterials Institute, Drexel University, Philadelphia, Pennsylvania 19104, United States

Supporting Information

ABSTRACT: Ti_3C_2 and other two-dimensional transition metal carbides known as MXenes are currently being explored for many applications involving intercalated ions, from electrochemical energy storage, to contaminant sorption from water, to selected ion sieving. We report here a systematic investigation of ion exchange in Ti_3C_2 MXene and its hydration/dehydration behavior. We have investigated the effects of the presence of LiCl during the chemical etching of the MAX phase Ti_3AlC_2 into MXene $Ti_3C_2T_x$ (T stands for surface termination) and found that the resulting MXene has Li^+ cations in the interlayer space. We successfully exchanged the Li^+ cations with K^+, Na^+, Rb^+, Mg^{2+}, and Ca^{2+} (supported by X-ray photoelectron and energy-dispersive spectroscopy) and found that the exchanged material expands on the unit-cell level in response to changes in humidity, with the nature of expansion dependent on the intercalated cation, similar to behavior of clay minerals; stepwise expansions of the basal spacing were observed, with changes consistent with the size of the H_2O molecule. Thermogravimetric analysis of the dehydration behavior of these materials shows that the amounts of H_2O contained at ambient humidity correlates simply with the hydration enthalpy of the intercalated cation, and that the diffusion of the exiting H_2O proceeds with kinetics similar to clays. These results have implications for understanding, controlling, and exploiting structural changes and H_2O sorption in MXene films and powders utilized in applications involving ions, such as electrochemical capacitors, sensors, reverse osmosis membranes, or contaminant sorbents.

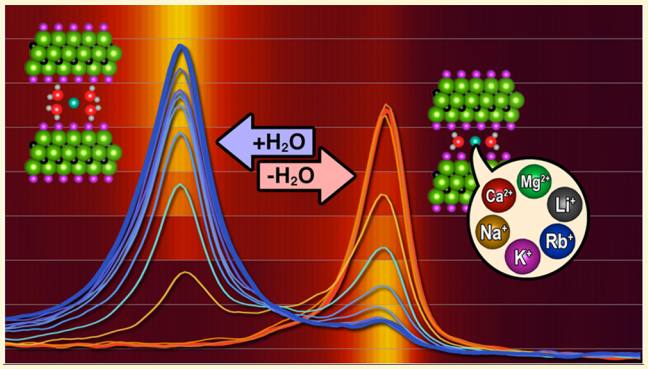

INTRODUCTION

MXenes—two-dimensional transition metal carbonitrides of the $M_{n+1}X_nT_x$ composition, where M is an early transition metal, X is carbon and/or nitrogen, n = 1, 2, or 3, and T represents a variable surface termination[1,2] such as O, OH, or F—are a rapidly growing class of materials featuring hydrophilicity, high electrical conductivity, and tunable chemistry and structure.[3,4] They have been explored in applications from energy storage to water purification to transparent conductive electrodes.[5−8] Furthermore, spontaneous intercalation of organic molecules (urea, hydrazine, DMF, etc.), as well as spontaneous and electrochemical intercalation of various cations (Li^+, Na^+, K^+, NH_4^+, Mg^{2+}, Al^{3+}) were previously reported.[9−11]

Understanding the intercalation chemistry of 2D materials is a prerequisite to many applications. Based on the ability to intercalate cations and the reversible increase in the c lattice parameter (c-LP) with H_2O uptake, MXenes have been compared with expanding clay minerals.[12] Although the reversible expansion of clay minerals in H_2O and the effects of cation exchange have been studied extensively, a fundamental study of the structural effects resulting from cation substitution in MXenes in aqueous, pH-neutral environments has not been undertaken. This is especially pertinent now that a number of MXene applications have been explored involving interactions with salt solutions; for example, when MXenes are used in supercapacitors with aqueous electrolytes,[10,13] as sorbents for Pb or Cr ions,[14,15] or membranes for ion sieving, the nature of the cation can play a large role in affecting the sorption efficiency or structure and permeability of the membranes.[6] It has been shown that spontaneous cation intercalation described in reference[10] may lead to changes in MXene surface chemistry,[16] but no systematic studies have been reported. If intercalated cations are structurally inherent in MXenes, controlling their concentrations and understanding their effects on interlayer separation can be crucial for tuning

Received: March 30, 2016
Revised: April 29, 2016

DOI: 10.1021/acs.chemmater.6b01275
Chem. Mater. XXXX, XXX, XXX−XXX

electrochemical energy storage, optical, and ion-exchange properties. The drastic changes noticed when Li^+ ions were presumably intercalated into the MXene structure during synthesis[12] led us to examine this more carefully in a model system, using $Ti_3C_2T_x$, to date the most widely studied and best understood MXene member.

The purpose of this work is to investigate cation substitutions and understand how they affect the interlayer spacing of MXenes. Herein, we describe a systematic study of the intercalation of alkali and alkaline earth cations and H_2O on the interlayer spacing of multilayer $Ti_3C_2T_x$ and how these cation-exchanged varieties respond to changes in relative humidity (RH).

EXPERIMENTAL SECTION

Synthesis of Ti_3AlC_2. Ti_2AlC powders (−325 mesh, Kanthal, Sweden) were mixed with TiC (Alfa Aesar, 99.5% purity) and heated to 1350 °C (at a heating rate of 10 °C/min following by a 2 h soak) to afford Ti_3AlC_2, according to previously reported procedures.[17] The resulting solid was milled with a milling bit and sieved (−400 mesh) to produce powders under 38 μm in size.

Synthesis of $Ti_3C_2T_x$ HF10. Ti_3AlC_2 powder (sieved to <38 μm particle size) was slowly added to 10 wt % hydrofluoric acid (HF) (Acros) in a ratio of 1 g Ti_3AlC_2:10 mL etching solution. The reaction mixture was stirred for 24 h at 25 °C, after which the powders were washed with distilled water in a centrifugation and decantation process: water was added to the reaction mixture, it was shaken for 1 min, then centrifuged for 2 min to collect the powders. The supernatant was then discarded, and the process repeated. This was done in a ratio of ∼0.5 g powders:40 mL water. Upon reaching a pH of ∼5, the powders were filtered to remove excess water and left for another 24 h to dry in air.

$Ti_3C_2T_x$ intercalated with ions. Similar to the above procedure, Ti_3AlC_2 powder was added to an etching mixture in the same ratio. In this case, however, the etchant was a mixture of 10% HF and LiCl. The etchant contained LiCl in a molar ratio 5 LiCl:1 Ti_3AlC_2. The mixture was stirred for 24 h at 25 °C followed by washing as described previously.

Acid Pre-washing. To remove traces of LiF precipitated during etching, the mixture was washed with a centrifugation procedure as described above, with three washes consisting of 6 M HCl (Fisher TraceMetal grade). This procedure was performed directly after the etching, before any of the sediments were allowed to dry.

Intercalation/Exchange. All samples were acid pre-washed as described above. Before the samples were allowed to dry, salt solutions (1 M LiCl, NaCl, KCl, RbCl; 0.5 M $MgCl_2$ or $CaCl_2$ in distilled water) were added in a ratio of roughly 0.5 g MXene:40 mL solution. After shaking for 2 min, the mixtures were allowed to sit for 1 h. The samples were then centrifuged to settle the powders, and the supernatants were decanted and replaced with fresh solutions. The samples were again shaken and allowed to sit for 24 h. Then they were centrifuged, the supernatants were discarded, and water was added, followed by agitation and centrifugation. After decanting, the sediment was collected via filtration, and washed with distilled water (2 × 5 mL) followed by drying in air (roughly 50% RH) to yield desired powders.

Characterization Techniques. *X-ray Diffraction (XRD).* A diffractometer (Rigaku SmartLab, Rigaku Corporation, Tokyo, Japan) was used to measure XRD patterns (Cu Kα radiation source). Samples were scanned at a step size of 0.04° and dwell time of 0.5 s per step. For measurements on fresh paste samples, before being allowed to dry, the paste was spread into a glass sample holder 0.2 mm deep with area of 4 cm^2 and flattened with a glass slide. Crystalline Si was added as an internal standard for calibrating angles.

XRD with Humidity Control. Measurements were carried out on a Bruker D8 Advance X-ray powder diffractometer under controlled humidity on a thin-layer slurry mount (quartz zero background) with ambient temperature of ∼23 °C. Samples were scanned at a step size of 0.02° and dwell time of 1.0 s per step. Each change in RH was accompanied by roughly 40 min of equilibration time prior to measurement.

X-ray Photoelectron Spectroscopy (XPS). A Physical Electronics VersaProbe 5000 instrument was used employing a 100 μm monochromatic Al Kα to irradiate the sample surface. Samples were in the form of cold pressed discs (pressed to ∼1 GPa). Photoelectrons were collected by a 180° hemispherical electron energy analyzer. Samples were analyzed at a 70° angle between the sample surface and the path to the analyzer. High-resolution spectra of Ti 2p, C 1s, O 1s, F 1s, Rb 3d, Na 1s, and Cl 2p were taken at a pass energy of 23.5 eV, with a step size of 0.05 eV, while for the Li 1s region the pass energy used was 11.7 eV, with the same step size. Post-sputtering spectra were taken after the samples were sputtered with an Ar beam operating at 3.8 kV and 150 μA for 30 min. All binding energies were referenced to that of the valence band edge at 0 eV.

Peak fitting for the high-resolution spectra was performed using CasaXPS Version 2.3.16 RP 1.6. Prior to the peak fitting the background contributions were subtracted using a Shirley function. For the Ti $2p_{3/2}$ and $2p_{1/2}$, Cl $2p_{3/2}$ and $2p_{1/2}$, and Rb $3d_{5/2}$ and $3d_{3/2}$ components, the intensity ratios of the peaks were constrained to be 2:1, 2:1, and 3:2, respectively. The global atomic percentage of the various elements was calculated using the following equation:

$$X_i = 100 \times \frac{A_i}{\sum_{j=1}^{m} A_j}$$

where X_i is the atomic concentration of the element i, A_i is the adjusted intensity of element i, and A_j is the total adjusted intensity of all elements. The adjusted intensity is defined as follows:

$$A_i = \frac{I_i}{R_i}$$

where I_i is the integrated peak area, and R_i is the relative sensitivity factor. The atomic percentages of the various species were determined by multiplying the total atomic percentage of each element by the fraction of that element. The total atomic percentage of each element was obtained from the high resolution spectra of that element. High-resolution spectra for Al 2p regions are not shown here.

Thermogravimetric Analysis (TGA). TGA was performed on a TA Instruments SDT 2960 Simultaneous DSC-TGA in alumina crucibles under dry nitrogen (Zero Grade 99.998%, passed through a molecular sieve drying column at 100 cm^3/min), with a standard of alumina powder. $Ti_3C_2T_x$ samples of 8−12 mg were used for each measurement.

RESULTS AND DISCUSSION

Material Production and Characterization. Figure 1 provides a general overview of materials in this report. We first produced $Ti_3C_2T_x$ by reaction of Ti_3AlC_2 powders with 10% HF as reported in ref 18 (denoted here as $Ti_3C_2T_x$ HF10). Full procedures are provided in the Supporting Information. After etching, removal of byproducts by washing with water, and drying, we attempted to intercalate Li by immersion in 1 M aqueous LiCl. Even after 72 h of exposure, no major changes (not shown) were observed in XRD patterns.

However, when LiCl was present as part of the etchant (5 molar equivalents per mole of Ti_3AlC_2)—rather than as a later addition—an intense and sharp 002 reflection, corresponding to a c-LP of 24.5 Å, was observed for the powder dried in ambient air (∼50% RH for 24 h), as opposed to the broader and less intense reflections of 19−20 Å often observed when only HF was used.[3,9,19] Some LiF was identified in XRD patterns of samples at this stage, most likely formed by precipitation through reaction of HF with LiCl.

We modified the washing procedure by adding initial washings of 6 M HCl to dissolve the LiF impurity. The material was then immersed in 1 M LiCl for 24 h to ensure that

DOI: 10.1021/acs.chemmater.6b01275
Chem. Mater. XXXX, XXX, XXX−XXX

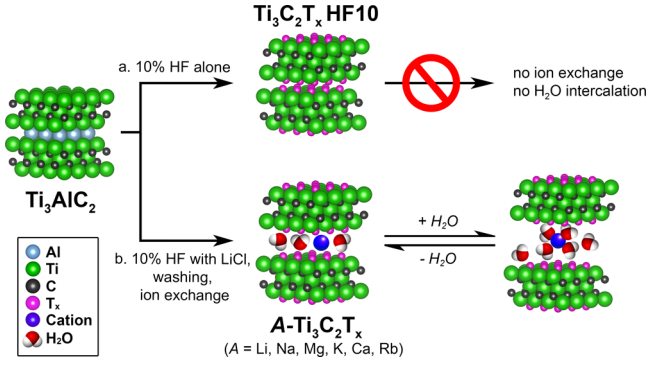

Figure 1. Pathway of materials prepared in this report. (a) Ti_3AlC_2 MAX phase is etched with 10% HF alone to remove Al and yield the MXene $Ti_3C_2T_x$ HF10 (T stands for a variable surface termination such as O, OH, F). This material does not show signs of intercalating cations or water. (b) When etched with 10% HF in the presence of LiCl and washed appropriately to remove excess salts, followed by ion exchange, a variety of intercalated MXenes denoted as A-$Ti_3C_2T_x$ are produced, where A is an intercalated cation. These materials co-intercalate H_2O reversibly to produce changes in basal spacing. Note that the illustrations are schematics and not precise structural models.

Li remained in the structure and that there was reduced chance for exchange with H^+. We designate this material Li-$Ti_3C_2T_x$. Figure 2 shows a comparison between the material etched with

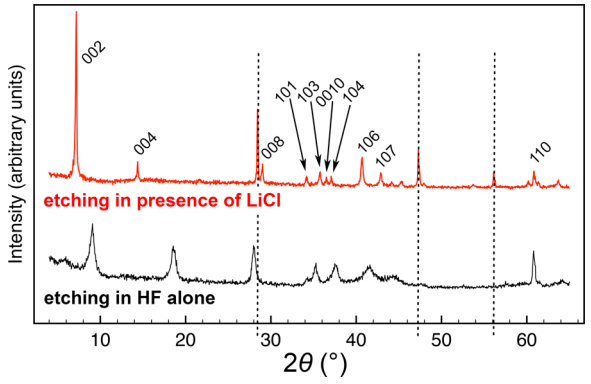

Figure 2. Effect of the presence of LiCl during etching: XRD patterns of $Ti_3C_2T_x$ HF10 (bottom) and Li-$Ti_3C_2T_x$ (top), showing higher structural order when Li^+ ions are present. Vertical dashed lines denote peaks from crystalline Si when included as an internal 2θ standard. All patterns were measured at ~40% RH.

HF alone ($Ti_3C_2T_x$ HF10, bottom trace) and when Li^+ ions were intercalated (Li-$Ti_3C_2T_x$, top trace). It is clear that the presence of Li^+ leads to greater structural order, and that the ions must be intercalated during etching. It is likely that randomly distributed H_2O molecules and varying surface group interactions cause much local variation in the basal spacing of $Ti_3C_2T_x$ HF10; a layer of dynamic H_2O and ions in the case of Li-$Ti_3C_2T_x$ could then cause the MXene sheets to be fixed at much more regular separations, leading to higher crystallinity.

To explore the intercalation of other ions, the material was prepared as described with HF and LiCl followed by washing with HCl; however, the final immersion in LiCl was replaced by immersion in 1 M solutions of NaCl, KCl, or RbCl, or 0.5 M solutions of $MgCl_2$ or $CaCl_2$. This was followed by washing with distilled water to remove traces of salts and drying in air to yield samples denoted as Na-$Ti_3C_2T_x$, K-$Ti_3C_2T_x$, Rb-$Ti_3C_2T_x$, Mg-$Ti_3C_2T_x$, and Ca-$Ti_3C_2T_x$.

We used XPS to evaluate our claims of ion intercalation, focusing on Li-$Ti_3C_2T_x$, Na-$Ti_3C_2T_x$, and Rb-$Ti_3C_2T_x$ as examples. A summary of changes specific to intercalated ions is given in Figure 3, and full data are given in Figures S4–S9

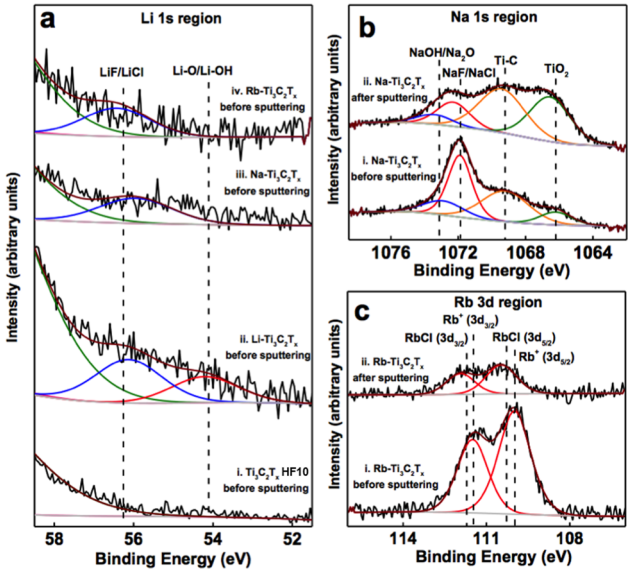

Figure 3. XPS spectra with curve-fitting. (a) Li 1s region for (i) $Ti_3C_2T_x$ HF10, (ii) Li-$Ti_3C_2T_x$, (iii) Na-$Ti_3C_2T_x$, (iv) Rb-$Ti_3C_2T_x$, all before sputtering. Dashed vertical lines represent, from left to right, species LiF/LiCl and LiOH/Li_2O; the large shoulder on the left is due to the Ti 3s peak (See Supporting Information for the complete region of the spectra, Figure S8 and Table S12). (b) Na 1s region for Na-$Ti_3C_2T_x$ (i) before and (ii) after sputtering. Dashed vertical lines, from left to right, represent the species NaOH (Na 1s), NaF/NaCl (Na 1s), Ti-C (Auger LMM line), and TiO_2 (Auger LMM line), respectively. (c) Rb 3d region for Rb-$Ti_3C_2T_x$ (i) before and (ii) after sputtering. Dashed vertical lines, from right to left, represent the species Rb^+ ($3d_{5/2}$), RbCl ($3d_{5/2}$), Rb^+ ($3d_{3/2}$), and RbCl ($3d_{3/2}$), respectively.

and Tables S5–S15. No Li-related peaks were present, either before or after sputtering, for $Ti_3C_2T_x$ HF10 (Figures 3a.i and S8.ii, respectively). However, for the Li-$Ti_3C_2T_x$ samples, the spectra before sputtering show the presence of two peaks, one corresponding to a LiF and/or LiCl species and one corresponding to Li–O and/or Li–OH species (Figure 3a.ii). The Li–O/Li–OH peak is at a binding energy (BE) of 54.2 eV (all values of the Li 1s region are presented in Table S12). This species probably originates from the presence of Li^+ ions interacting with H_2O or with MXene-bound O-containing groups.[20] From the Li–O/Li–OH peak ratios before sputtering, the amount of Li^+ ions is estimated to be ~0.3 mol per mole of Ti_3C_2. The LiCl/LiF peak, at a BE of 56.1 eV, is due to residues from etching, where some LiF and/or LiCl salts were not completely removed. After sputtering, the two peaks corresponding to Li–O/Li–OH and LiCl/LiF (Figure S8.iv) were replaced by one, at a BE of 55.8 eV (which lies between those for the two species), with the same full-width at half-maximum (fwhm) as the peaks for those species before sputtering. This peak shift might be due to the effect of sputtering on the Li species.

Figure 3b.i and b.ii shows XPS spectra for the Na 1s region for Na-$Ti_3C_2T_x$, before and after sputtering, respectively. This region was fit by four species, one each to NaF/NaCl and NaOH/Na_2O.[21–23] The former likely results from incomplete washing of NaCl salts and the possible formation of NaF. The

DOI: 10.1021/acs.chemmater.6b01275
Chem. Mater. XXXX, XXX, XXX–XXX

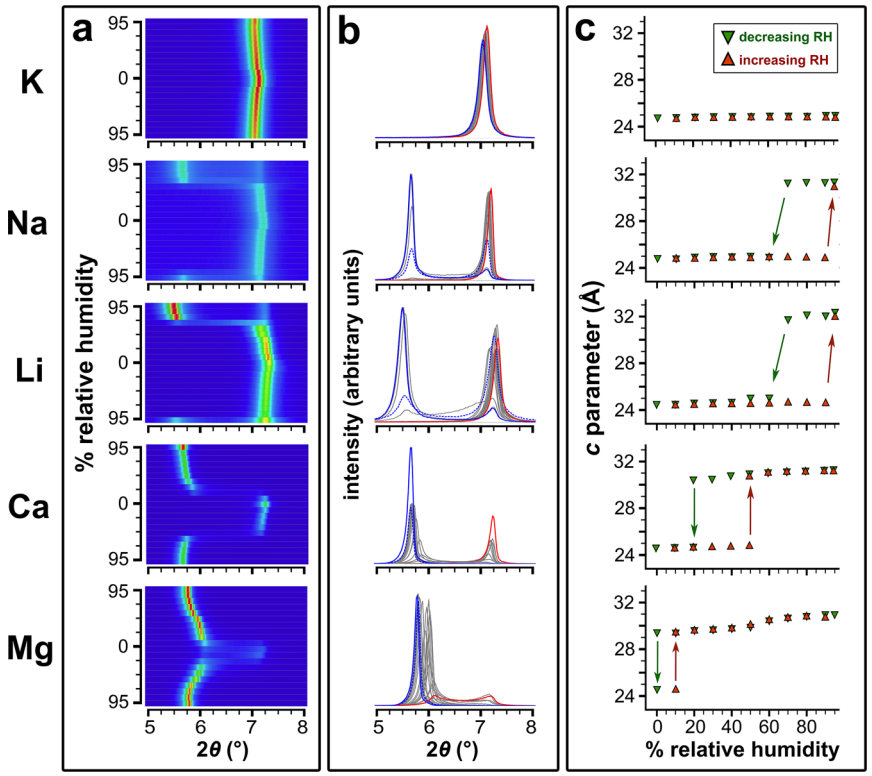

Figure 4. (a) 3D plots of the 002 region of A-$Ti_3C_2T_x$ (with each intercalated cation A denoted at left) as RH was varied from 95% to ~0 and back to 95%. The color scheme represents diffraction intensity, with red being highest and blue lowest. (b) The same data, where the peaks are superimposed and presented as intensity versus 2θ plots, to better illustrate the shape of the diffraction peaks used to generate the 3D plots. Solid blue traces denote the initial condition at 95% RH, red traces denote the material at 0% RH, and dashed blue traces denote the material after return to 95% RH. (c) The c parameter ($2 \times d_{002}$) extracted from the peaks shown in panels a and b, as a function of RH. Green down triangles represent the path from 95% to 0% RH and red up triangles the path from 0% to 95% RH following the down path. Data are organized by intercalated cation in order of increasing hydration enthalpy.

latter likely originates from intercalated Na^+ ions. The other two species originate from the Ti LMM Auger lines and correspond to the Ti−C species in MXene and TiO_2 (surface oxides).[24] It is worth noting that the BE of all these species shifts to a slightly higher BE (about 0.1−0.2 eV) after sputtering. Again, this might be an effect of the sputtering process. The amount of Na^+ intercalant per mole of Ti_3C_2, estimated from the XPS spectra, was ~0.24 mol (before sputtering). XPS spectra of the Li 1s region for Na-$Ti_3C_2T_x$ before sputtering (Figure 3a.iii) show no sign of Li−O/Li−OH species, with only a peak for LiF/LiCl species. This holds true after sputtering as well (Figure S8.vi). The lack of a peak corresponding to intercalated Li^+ suggests complete exchange between Li^+ and Na^+ ions. XPS spectra of the Rb-$Ti_3C_2T_x$ samples were similar; the disappearance of the Li^+ species in the Li 1s region (Figures 3a.iv and S8.viii) is associated with the appearance of a species in the Rb 3d region (Figure 3c).[25] The amount of Rb species intercalated per mole of Ti_3C_2, estimated from the XPS spectra, was ~0.16 mol (before sputtering). A summary of the MXene chemistries obtained from the XPS peak fittings in a similar manner as in ref 1 is shown in Table S7.

We did not carry out XPS measurements on K-$Ti_3C_2T_x$, Mg-$Ti_3C_2T_x$, or Ca-$Ti_3C_2T_x$. Energy-dispersive X-ray spectroscopy (EDS) of these and other samples supported the presence of cations without proportionate amounts of Cl (Figure S1 and Table S1). From these data, we determined approximate cation amounts per Ti_3C_2 for Na-, Mg-, K-, and Rb-$Ti_3C_2T_x$ to be ~0.18, 0.08, 0.17, and 0.25, respectively. The amount of Cl was consistent across all samples and is probably present as a chloride salt impurity or a minor surface termination.

It is difficult to compare the cation amounts obtained from XPS with those obtained from EDS, as XPS is more surface-sensitive and considers different species, whereas EDS has a greater penetration depth but insufficient resolution to distinguish various species. Given these differences between the two methods, we find agreement to be mostly reasonable. As discussed below, the varied responses of these MXenes to humidity is strong evidence for the intercalation of K, Mg, and Ca.

In Situ XRD with Humidity Control. It is well established that many clay materials exhibit different structural responses to changes in relative humidity or water activity.[26,27] As this has not yet been explored in MXene, we set out to characterize the response of ion-exchanged $Ti_3C_2T_x$ to changes in RH, using XRD to track the 00l reflections (related to the c-LP). For this study we measured the samples K-$Ti_3C_2T_x$, Li-$Ti_3C_2T_x$, Na-$Ti_3C_2T_x$, Mg-$Ti_3C_2T_x$, and Ca-$Ti_3C_2T_x$. RH was varied between ~0 and 95%, with ~40 min given for equilibration before each measurement. The results are shown in Figure 4. The 3D plots in Figure 4a show how the 2θ of the 002 reflection for Ti_3C_2 exchanged with various cations shifted as the RH dropped from 95% to ~0% and then increased again to the initial humidity. The same data are presented superimposed as more typical intensity vs 2θ XRD patterns in Figure 4b so that the shape of the peaks can be seen. The positions of the reflections, at

DOI: 10.1021/acs.chemmater.6b01275
Chem. Mater. XXXX, XXX, XXX−XXX

maximum intensity, are summarized as a function of RH in Figure 4c. It is immediately clear that (1) the reflections do not shift continuously, i.e., there are only two major reflections, with no peaks in between, and (2) different cations result in very different responses.

The *c* of all samples at ~0% RH is roughly 25 Å, which contrasts with that of MXene under similar conditions produced using HF alone—viz. $Ti_3C_2T_x$ HF10—at ~20 Å,[2] a difference corresponding roughly to the diameter of an H_2O molecule. We believe this 25 Å phase is intercalated with a single layer of H_2O molecules (this type of structure has been suggested for MXenes previously[28]). Almost all samples, with the exception of K-$Ti_3C_2T_x$, experienced a discontinuous shift in *c* at high humidities of the order of +3 Å per interlayer, most probably due to the presence of a bilayer H_2O structure, as has been observed in other materials.[29−31]

These results imply that the RH at which expansion from the monolayer structure occurs is related to the hydration enthalpy of the cation (Table S2), with the K^+ samples showing almost no expansion and the Mg^{2+} samples showing almost no single H_2O layer form until very low humidities. The simplest physical explanation is that there is an energy requirement to separate the $Ti_3C_2T_x$ sheets, which is overcome by the hydration of the intercalated cation; the divalent cations have a sufficiently high driving force (related to hydration enthalpy) to form a bilayer H_2O structure in the MXene interlayer at moderate humidity, whereas Li^+ and Na^+ require higher RH due to their lower hydration energies, and K^+ is unable to stabilize a bilayer. This behavior is parallel with the behavior noted in numerous studies of smectites, showing a direct link to hydration energy of interlayer cations, with a secondary effect from the charge on the individual silicate layers.[32,33] In addition, XRD data, for all but the K-exchanged sample, reveal significant hysteresis between the hydration and dehydration branches, which is also consistent with this suggested hydration behavior. This can be seen, for example, in the marked difference in the RH value required for Ca-$Ti_3C_2T_x$ to change between the monolayer and bilayer structure on hydration (~50% RH) and dehydration (~20% RH). To confirm that no other major structural changes were occurring between hydration and dehydration, full XRD patterns including the *hkl* 2θ regions were recorded for Ca-$Ti_3C_2T_x$ at 95% and ~0% RH and are reported in Figure S2. There is no change in the position of the 110 peak, signifying no change of structure along the direction parallel to the basal planes.[12]

Finally, in a separate experiment, Li-$Ti_3C_2T_x$ was saturated with liquid water and allowed to equilibrate in an ambient atmosphere of ~40% RH while XRD patterns were recorded roughly every 4 min as the liquid water evaporated; these are presented as a 3D plot in Figure 5. This provides some insight into the time scale—roughly an hour—of the bilayer-to-monolayer transformation at a typical ambient RH. Further, this experiment demonstrates conclusively that the transition involves a discontinuous jump in c-LP: any continuous change that could hide during the equilibrations between measurements in the RH-controlled XRD (Figure 4) would be apparent here.

Thermogravimetric Analysis. To evaluate the connection between the expansion of the layers and the amount of intercalated H_2O, we performed TGA on select representative samples (Li-$Ti_3C_2T_x$, Na-$Ti_3C_2T_x$, K-$Ti_3C_2T_x$, and Ca-$Ti_3C_2T_x$) (Figure 6). All samples were first equilibrated at ~50% RH at 25 °C, and TGA was subsequently performed in

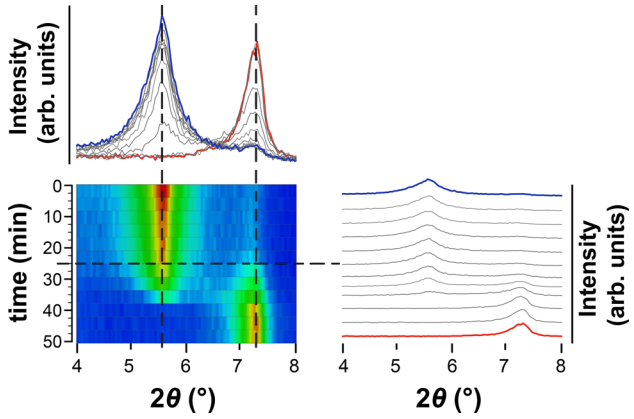

Figure 5. 3D plot for dehydration of initially wet Li-$Ti_3C_2T_x$ in an environment of ~40% RH and 25 °C. The heat plot is composed of XRD patterns where red represents the highest diffraction intensity and blue the lowest. The original patterns are shown superimposed (above) and stacked (right) for clarity on the construction of the heat plot. The blue XRD pattern represents Li-$Ti_3C_2T_x$ in the presence of liquid water, and the red plot is the pattern once the transition has completed.

various temperature steps (Figure 6a), ramping stepwise up to 120 °C. In order to compare and interpret results, we made the assumption that most of the H_2O associated with cations—i.e., H_2O of hydration—was removed after heating using the temperature program shown in Figure 6a. Normalizing the weight loss results by the weight 250 min after the start of the experiments gave the mass-loss curves shown in Figure 6a. Each sample was maintained at ~27 °C under a 100 cm^3/min flow of dry N_2 for the first segment in the temperature program. We compared TGA and XRD data for each sample under comparable conditions to formulate a structural model for dehydration; the material should undergo the same changes during TGA from its initial state (50% RH, 25 °C) to the end of the first step (~0% RH, 27 °C) as it did over the same RH range in XRD experiments. In other words, the fact that Ca-$Ti_3C_2T_x$ has the highest mass loss during this step is consistent with it having the greatest Δc-LP as seen from XRD (taken to be an H_2O bilayer-to-monolayer transition). The TGA data show that all samples lose H_2O, even without major change in *c* (in the case of K^+, Na^+, and Li^+ samples), so it is important to address whether the desorbed H_2O originates from the interlayer (leading to structural changes observable in XRD) or from surface-adsorbed water outside the particles. Based on work on clay minerals,[34] we believe that, after equilibration at 50% RH, the dominant contribution to desorbable H_2O will come from the interlayer, rather than interparticle pores or surface-adsorbed H_2O (see Figure S3 for a typical distribution of particle sizes; the particles should be large enough that their outside surface area is much smaller relative to the amount of interlayer space).

Further, sample Ca-$Ti_3C_2T_x$ demonstrates a clear discontinuous bilayer-to-monolayer transition at low RH but a more continuous change in the weight loss at 27 °C; we believe that as H_2O evolves from the structure, pillars of hydrated cations remain until the abrupt transition, at which point H_2O supporting the expanded structure is removed, leaving monolayer H_2O between the collapsed basal planes.

A plot of the normalized mass fraction against ion hydration enthalpy is nearly linear (Figure 6b), strongly supporting the idea that the bulk of the H_2O initially present in the structure at

DOI: 10.1021/acs.chemmater.6b01275
Chem. Mater. XXXX, XXX, XXX−XXX

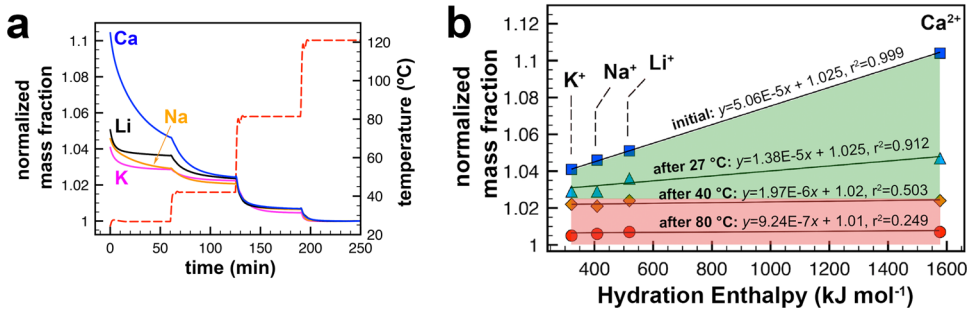

Figure 6. (a) Temperature during the TGA runs, showing the stepwise programming, beginning at 27 °C and ramping to 40 °C, 80 °C, and 120 °C with 1 h of equilibration time during each step (right axis). Data are not smoothed. Mass fraction for selected ion-intercalated samples is shown on the left axis. All mass changes were normalized by their mass after 250 min from the start of heating, assuming that most H_2O had been removed at that point. (b) The same mass fraction data from (a) initially, and after equilibration steps, plotted against cation hydration enthalpy. Linear regression fits are shown above each data set. The green shaded area represents mass loss more strongly correlated with ion hydration enthalpy, and the red shaded area represents loss of additional H_2O. Note that the x-axis begins at 200 kJ/mol.

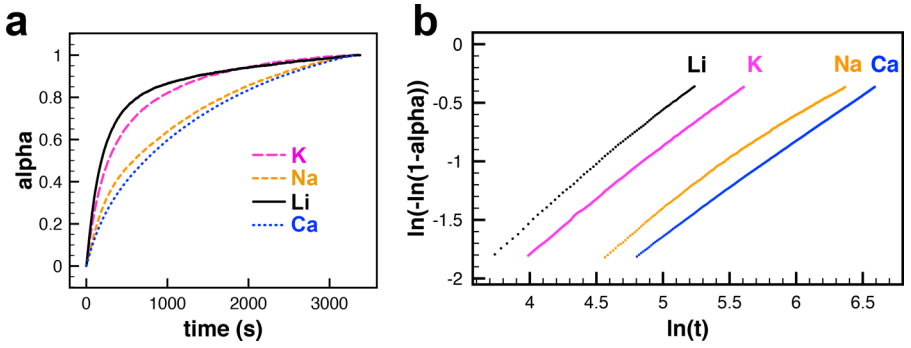

Figure 7. (a) Plot of α against time at 27 °C for K-$Ti_3C_2T_x$, Na-$Ti_3C_2T_x$, Li-$Ti_3C_2T_x$, and Ca-$Ti_3C_2T_x$. (b) Linearization of data from (a) in Avrami analysis to extract k and m values.

50% RH is hydrating the cations. After initial dehydration at 27 °C, samples were equilibrated at 40 °C, and after this step, there was no longer a strong dependence on the hydration enthalpy, which can clearly be seen after 80 °C equilibration. Linear fits to the initial and 27 °C data share the y-intercept; the plot in Figure 6b is divided into regions that show strong dependence on cations (green shaded area) and further weight loss (red shaded area) that is attributed to H_2O adsorbed to MXene surfaces. Considering the H_2O lost in the region that shows strong dependence on cation hydration enthalpy, we estimate the number of H_2O per Ti_3C_2 formula unit at 50% RH to be 0.18, 0.24, 0.29, and 0.91 for $Ti_3C_2T_x$ intercalated with K^+, Na^+, Li^+, and Ca^{2+}, respectively. We note that these values fall within a range observed for similar materials.[30,35] Full data for this derivation are provided in Tables S3 and S4. Some samples from the diffraction study were not used in the TGA study due to time constraints, but we feel that the ion-intercalated samples selected give a representative picture.

Bray and Redfern[36] applied the Avrami equation to thermal analysis data for Ca-montmorillonite, an expanding clay mineral intercalated with Ca^{2+}, to determine the kinetics and mechanism of diffusion of H_2O from the structure. The equation

$$\ln(-\ln(1-\alpha)) = m \ln k + m \ln t$$

where t is time in seconds and α is the extent of reaction (a value from 0 to 1), can be used with weight loss data. The rate constant k and a parameter related to the reaction mechanism, m, can be extracted from the slope and intercepts (k and k ln m, respectively). Bray and Redfern found that, for dehydration at 20 and 30 °C in a dry N_2 atmosphere, their Ca-montmorillonite gave m values between 0.6, associated with 2D diffusion-controlled reactions, and 1.0, associated with a first-order process; they suggested a first-order process that was slowed by diffusion through the interlayers.

Plots of α vs time for our materials are shown in Figure 7a (derived by taking the initial mass percent at a given temperature step as α = 0 and the mass percent at near equilibrium as α = 1). Linearizations according to the equation above are plotted in Figure 7b to extract k and m (for these, α was taken between 0.15 and 0.5). Our data at 27 °C provide k and m values of, respectively, 0.0025, 0.88 (K-$Ti_3C_2T_x$); 0.0011, 0.78 (Na-$Ti_3C_2T_x$); 0.0037, 0.95 (Li-$Ti_3C_2T_x$); and 0.00097, 0.80 (Ca-$Ti_3C_2T_x$). The values for Ca-$Ti_3C_2T_x$ compare favorably with those of Bray and Redfern's Ca-montmorillonite, namely 0.0008, 0.99 at 20 °C and 0.0033, 0.86 at 30 °C. Based on the similarity between the values of these parameters for our material and Ca-montmorillonite, it is reasonable to conclude that a similar process of H_2O loss from the interlayers is occurring in our samples. However, more careful work—with controlled particle sizes, and various controlled atmospheres—is needed to fully understand the dehydration mechanisms. These initial findings on the kinetics of dehydration should help shape decisions made in material processing and handling in terms of how to control water content.

It is significant that our observations are in agreement with the behavior observed for other layered materials, such as clays and sulfides of transition metals. The layered ternary sulfides are likely better analogs to MXenes than swelling clays in terms of properties and applications, because some of them are

DOI: 10.1021/acs.chemmater.6b01275
Chem. Mater. XXXX, XXX, XXX−XXX

electrically conductive, whereas clays are chemically closer to MXenes due to their O/OH surface terminations. Lerf and Schöllhorn studied solvation effects of A_xTiS_2, A_xNbS_2, and A_xTaS_2, where A is a group-1 or group-2 cation.[29] They found that c-LP expansion could be related to the hydration properties of the various A cations and were weak functions of the transition metal, viz., Ti, Nb, or Ta. This suggests that MXenes containing other transition metals (V, Nb, Mo, Ta, etc.[4]) may behave similarly to $Ti_3C_2T_x$, even though this comparison should be verified by experiments. Lerf and Schöllhorn also documented discrete hydration stages that depended on the activity of H_2O, corresponding to monolayers or bilayers of intercalated H_2O, as has been extensively documented for swelling clay minerals. Whittingham also observed similar behavior in terms of cation hydration.[37] Most notable in these systems (and in swelling clay systems), especially the Ti-based dichalcogenides, is that Li^+, Na^+, and the divalent cations are able to stabilize H_2O bilayers, which is exactly the case observed here for $Ti_3C_2T_x$.

CONCLUSIONS

We have demonstrated that etching of Ti_3AlC_2 to produce $Ti_3C_2T_x$ with the combination of HF and LiCl can yield MXenes with different characteristics than those produced with HF alone, and we provide evidence that this material behaves like swelling clay minerals and metal dichalcogenides. Through XPS and EDS analyses, we demonstrate the cation exchange of Li^+ with Na^+, K^+, Rb^+, Mg^{2+}, and Ca^{2+}. These cations, in turn, give rise to quite different structural changes in response to RH, as evidenced by XRD, involving a discontinuous structural expansion in the direction normal to the basal plane as H_2O molecules intercalate. TGA data support the idea that the expansion is caused by H_2O associated with the cations, and the excellent correlation with hydration enthalpy supports the conclusion that this H_2O lost originates from hydration of alkali metal ions intercalated between the MXene layers. Further, Avrami-type analysis of the TGA data suggests reaction mechanisms in agreement with these reported for Ca-montmorillonite, a swelling clay with surface functionalities similar to MXene.

The findings from this study potentially impact the use of MXenes in many applications. For electrochemical energy storage, the ion permeability and hence rate performance is related to the interlayer spacing of the MXene sheets; the results here may guide the rational selection of electrolytes or the initial ion composition of the starting MXene. For applications involving water purification or desalination, interations with other ions in the solution (for example, municipal water or seawater), especially involving the structural changes or durability of MXene films, will be important considerations. Finally, due to MXene's inherent high conductivity, we imagine applications in which the conductivity can be modulated in response to changing RH.

ASSOCIATED CONTENT

Supporting Information

The Supporting Information is available free of charge on the ACS Publications website at DOI: 10.1021/acs.chemmater.6b01275.

EDS, SEM, additional XRD patterns, TGA, and full XPS data (PDF)

AUTHOR INFORMATION

Corresponding Author

*E-mail: barsoumw@drexel.edu.

Notes

The authors declare no competing financial interest.

ACKNOWLEDGMENTS

This work was supported by the U.S. National Science Foundation under Grant No. DMR-1310245; M.G. was supported by the National Science Foundation Graduate Research Fellowship under Grant 283036-3304. J.H. was supported through the Swedish Research Council (Project Grant No. 621-2014-4890), the Swedish Foundation for Strategic Research through the Synergy Grant FUNCASE Functional Carbides for Advanced Surface Engineering. We thank the Drexel Core Facility and staff for assistance with characterization involving SEM, EDS, XRD, and XPS. Collaboration between Drexel University and Indiana University was supported by the Fluid Interface Reactions, Structures and Transport (FIRST) Center, an Energy Frontier Research Center funded by the U.S. Department of Energy, Office of Science, Office of Basic Energy Sciences. The authors are grateful to Dr. David J. Wesolowski and Dr. Hsiu-Wen Wang from the Oak Ridge National Laboratory, who initiated this collaboration, for help and discussions.

REFERENCES

(1) Halim, J.; Cook, K. M.; Naguib, M.; Eklund, P.; Gogotsi, Y.; Rosen, J.; Barsoum, M. W. X-Ray Photoelectron Spectroscopy of Select Multi-Layered Transition Metal Carbides (MXenes). *Appl. Surf. Sci.* **2016**, *362*, 406−417.

(2) Wang, H.-W.; Naguib, M.; Page, K.; Wesolowski, D. J.; Gogotsi, Y. Resolving the Structure of $Ti_3C_2T_x$ MXenes through Multilevel Structural Modeling of the Atomic Pair Distribution Function. *Chem. Mater.* **2016**, *28*, 349−359.

(3) Naguib, M.; Mashtalir, O.; Carle, J.; Presser, V.; Lu, J.; Hultman, L.; Gogotsi, Y.; Barsoum, M. W. Two-Dimensional Transition Metal Carbides. *ACS Nano* **2012**, *6*, 1322−1331.

(4) Naguib, M.; Mochalin, V. N.; Barsoum, M. W.; Gogotsi, Y. 25th Anniversary Article: MXenes: A New Family of Two-Dimensional Materials. *Adv. Mater.* **2014**, *26*, 992−1005.

(5) Xie, Y.; Dall'Agnese, Y.; Naguib, M.; Gogotsi, Y.; Barsoum, M. W.; Zhuang, H. L.; Kent, P. R. C. Prediction and Characterization of MXene Nanosheet Anodes for Non-Lithium-Ion Batteries. *ACS Nano* **2014**, *8*, 9606−9615.

(6) Ren, C. E.; Hatzell, K. B.; Alhabeb, M.; Ling, Z.; Mahmoud, K. A.; Gogotsi, Y. Charge- and Size-Selective Ion Sieving Through $Ti_3C_2T_x$ MXene Membranes. *J. Phys. Chem. Lett.* **2015**, *6*, 4026−4031.

(7) Halim, J.; Lukatskaya, M. R.; Cook, K. M.; Lu, J.; Smith, C. R.; Näslund, L.-Å.; May, S. J.; Hultman, L.; Gogotsi, Y.; Eklund, P.; Barsoum, M. W. Transparent Conductive Two-Dimensional Titanium Carbide Epitaxial Thin Films. *Chem. Mater.* **2014**, *26*, 2374−2381.

(8) Yu, Y.-X. Prediction of Mobility, Enhanced Storage Capacity, and Volume Change during Sodiation on Interlayer-Expanded Functionalized Ti_3C_2 MXene Anode Materials for Sodium-Ion Batteries. *J. Phys. Chem. C* **2016**, *120*, 5288−5296.

(9) Mashtalir, O.; Naguib, M.; Mochalin, V. N.; Dall'Agnese, Y.; Heon, M.; Barsoum, M. W.; Gogotsi, Y. Intercalation and Delamination of Layered Carbides and Carbonitrides. *Nat. Commun.* **2013**, *4*, 1716.

(10) Lukatskaya, M. R.; Mashtalir, O.; Ren, C. E.; Dall'Agnese, Y.; Rozier, P.; Taberna, P. L.; Naguib, M.; Simon, P.; Barsoum, M. W.; Gogotsi, Y. Cation Intercalation and High Volumetric Capacitance of Two-Dimensional Titanium Carbide. *Science* **2013**, *341*, 1502−1505.

(11) Levi, M. D.; Lukatskaya, M. R.; Sigalov, S.; Beidaghi, M.; Shpigel, N.; Daikhin, L.; Aurbach, D.; Barsoum, M. W.; Gogotsi, Y.

DOI: 10.1021/acs.chemmater.6b01275
Chem. Mater. XXXX, XXX, XXX−XXX

Solving the Capacitive Paradox of 2D MXene Using Electrochemical Quartz-Crystal Admittance and In Situ Electronic Conductance Measurements. *Adv. Energy Mater.* **2015**, *5*, 1400815.
(12) Ghidiu, M.; Lukatskaya, M. R.; Zhao, M.-Q.; Gogotsi, Y.; Barsoum, M. W. Conductive Two-Dimensional Titanium Carbide "clay" with High Volumetric Capacitance. *Nature* **2014**, *516*, 78−81.
(13) Wang, X.; Kajiyama, S.; Iinuma, H.; Hosono, E.; Oro, S.; Moriguchi, I.; Okubo, M.; Yamada, A. Pseudocapacitance of MXene Nanosheets for High-Power Sodium-Ion Hybrid Capacitors. *Nat. Commun.* **2015**, *6*, 6544.
(14) Ying, Y.; Liu, Y.; Wang, X.; Mao, Y.; Cao, W.; Hu, P.; Peng, X. Two-Dimensional Titanium Carbide for Efficiently Reductive Removal of Highly Toxic Chromium(VI) from Water. *ACS Appl. Mater. Interfaces* **2015**, *7*, 1795−1803.
(15) Peng, Q.; Guo, J.; Zhang, Q.; Xiang, J.; Liu, B.; Zhou, A.; Liu, R.; Tian, Y. Unique Lead Adsorption Behavior of Activated Hydroxyl Group in Two-Dimensional Titanium Carbide. *J. Am. Chem. Soc.* **2014**, *136*, 4113−4116.
(16) Dall'Agnese, Y.; Lukatskaya, M. R.; Cook, K. M.; Taberna, P.-L.; Gogotsi, Y.; Simon, P. High Capacitance of Surface-Modified 2D Titanium Carbide in Acidic Electrolyte. *Electrochem. Commun.* **2014**, *48*, 118−122.
(17) Naguib, M.; Kurtoglu, M.; Presser, V.; Lu, J.; Niu, J.; Heon, M.; Hultman, L.; Gogotsi, Y.; Barsoum, M. W. Two-Dimensional Nanocrystals Produced by Exfoliation of Ti_3AlC_2. *Adv. Mater.* **2011**, *23*, 4248−4253.
(18) Ying, Y.; Liu, Y.; Wang, X.; Mao, Y.; Cao, W.; Hu, P.; Peng, X. Two-Dimensional Titanium Carbide for Efficiently Reductive Removal of Highly Toxic Chromium(VI) from Water. *ACS Appl. Mater. Interfaces* **2015**, *7*, 1795−1803.
(19) Gao, Y.; Wang, L.; Li, Z.; Zhou, A.; Hu, Q.; Cao, X. Preparation of MXene-Cu_2O Nanocomposite and Effect on Thermal Decomposition of Ammonium Perchlorate. *Solid State Sci.* **2014**, *35*, 62−65.
(20) Ren, C. E.; Zhao, M.-Q.; Makaryan, T.; Halim, J.; Boota, M.; Kota, S.; Anasori, B.; Barsoum, M. W.; Gogotsi, Y. Porous Two-Dimensional Transition Metal Carbide (MXene) Flakes for High-Performance Li-Ion Storage. *ChemElectroChem.* **2016**, DOI: 10.1002/celc.201600059.
(21) Citrin, P. H. High-Resolution X-Ray Photoemission from Sodium Metal and Its Hydroxide. *Phys. Rev. B* **1973**, *8*, 5545−5556.
(22) Nefedov, V. I.; Salyn, Y. V.; Leonhardt, G.; Scheibe, R. A Comparison of Different Spectrometers and Charge Corrections Used in X-Ray Photoelectron Spectroscopy. *J. Electron Spectrosc. Relat. Phenom.* **1977**, *10*, 121−124.
(23) Barrie, A.; Street, F. J. An Auger and X-Ray Photoelectron Spectroscopic Study of Sodium Metal and Sodium Oxide. *J. Electron Spectrosc. Relat. Phenom.* **1975**, *7*, 1−31.
(24) Briggs, D.; Seah, M. P. *Practical Surface Analysis, Auger and X-Ray Photoelectron Spectroscopy*; Wiley, 1990.
(25) Guo, C.; Yin, S.; Dong, Q.; Sato, T. Near-Infrared Absorption Properties of Rb_xWO_3 Nanoparticles. *CrystEngComm* **2012**, *14*, 7727−7732.
(26) Norrish, K. The Swelling of Montmorillonite. *Discuss. Faraday Soc.* **1954**, *18*, 120−134.
(27) Hou, X.; Bish, D. L.; Wang, S.-L.; Johnston, C. T.; Kirkpatrick, R. J. Hydration, Expansion, Structure, and Dynamics of Layered Double Hydroxides. *Am. Mineral.* **2003**, *88*, 167−179.
(28) Ghidiu, M.; Naguib, M.; Shi, C.; Mashtalir, O.; Pan, L. M.; Zhang, B.; Yang, J.; Gogotsi, Y.; Billinge, S. J. L.; Barsoum, M. W. Synthesis and Characterization of Two-Dimensional Nb_4C_3 (MXene). *Chem. Commun.* **2014**, *50*, 9517−9520.
(29) Lerf, A.; Schöllhorn, R. Solvation Reactions of Layered Ternary Sulfides A_xTiS_2, A_xNbS_2, and A_xTaS_2. *Inorg. Chem.* **1977**, *16*, 2950−2956.
(30) Foo, M. L.; Klimczuk, T.; Cava, R. J. Hydration Phase Diagram for Sodium Cobalt Oxide $Na_{0.3}CoO_2{\cdot}yH_2O$. *Mater. Res. Bull.* **2005**, *40*, 665−670.
(31) Sasaki, T.; Komatsu, Y.; Fujiki, Y. Protonated Pentatitanate: Preparation, Characterizations and Cation Intercalation. *Chem. Mater.* **1992**, *4*, 894−899.
(32) Chipera, S. J.; Carey, J. W.; Bish, D. L. *Controlled-Humidity XRD Analyses: Application to the Study of Smectite Expansion/Contraction*; Advances in X-ray Analysis *39*; Plenum Press, 1997; pp 713−722.
(33) Bish, D. L. Parallels and Distinctions between Clays and Zeolites. In *Handbook of Clay Science*; Elsevier, 2013; pp 243−345.
(34) Salles, F.; Beurroies, I.; Bildstein, O.; Jullien, M.; Raynal, J.; Denoyel, R.; Damme, H. V. A Calorimetric Study of Mesoscopic Swelling and Hydration Sequence in Solid Na-Montmorillonite. *Appl. Clay Sci.* **2008**, *39*, 186−201.
(35) Johnston, D. Ambient Temperature Phase Relations in the System $Na_{1/3}(H_2O)_yTaS_2$ ($0 < y < 2$). *Mater. Res. Bull.* **1982**, *17*, 13−23.
(36) Bray, H. J.; Redfern, S. A. T. Kinetics of Dehydration of Ca-Montmorillonite. *Phys. Chem. Miner.* **1999**, *26*, 591−600.
(37) Whittingham, M. S. The Hydrated Intercalation Complexes of the Layered Disulfides. *Mater. Res. Bull.* **1974**, *9*, 1681−1689.

DOI: 10.1021/acs.chemmater.6b01275
Chem. Mater. XXXX, XXX, XXX−XXX